Abraham N. Varghese
Naval Undersea Warfare Center Division
Newport, RI

James S. Uhlman

Ivan N. Kirschner

Anteon Corporation Engineering, Engineering Technology Center
Mystic, CT

Numerical Analysis of High-Speed Bodies in Partially Cavitating Axisymmetric Flow

Partial cavitation of high-speed axisymmetric bodies is modeled using a steady potential-flow boundary-element technique. The effects of several key parameters defining the vehicle geometry are examined for configurations consisting of a disk cavitator followed by a conical section and ending in a cylindrical body. A single cavity is assumed to detach at the edge of the disk. A variety of conditions have been studied, including cavity closure on either the conical or cylindrical portions of the vehicle, variations in the cone angle, and variations in the radius of the cylindrical section. The results for the partially cavitating case are also compared with those for the supercavitating case.
[DOI: 10.1115/1.1852473]

Introduction

At sufficiently high-speeds, cavitation will occur on the surface of submerged bodies at the point where the local pressure drops to the value of the vapor pressure of the ambient fluid. If the cavitation number is sufficiently low, a supercavity will form that covers the entire vehicle. Partial cavitation occurs for such bodies at lower speeds, for example, those characterizing a launch transient. Partial cavitation may also occur during flight when maneuvering of the vehicle is necessary. Partial cavities can be created or their extent increased via the use of suitably designed ventilation systems.

Early research on supercavitating flows was performed by Efros [1], who employed conformal mapping techniques. Tulin [2] introduced the use of perturbation methods for examination of two-dimensional supercavitating flows. Cuthbert and Street [3] used sources and sinks along the axis of a slender axisymmetric body-cavity system, along with a Riabouchinski cavity closure model. They solved for the unknown cavity shape, but were successful only for a few cases. Brennan [4] employed a relaxation method in a transformed velocity potential-stream function plane for analyzing axisymmetric cavitating flows behind a disk and a sphere between solid walls. Chou [5] extended the work of Cuthbert and Street [3] to solve axisymmetric supercavitating flows using slender body theory. He solved the problem by locating sources along the body-cavity axis and control points along the body-cavity surface. A nonlinear integro-differential equation was formed by imposing the dynamic condition on the cavity boundary. He assumed a conical cavity profile near closure to simplify the equation.

Vorus [6] addressed the problem of supercavitating flows using a Laurent series for the cavity shape, resulting in a more realistic cavity closure model, being the lowest-order representation of a re-entrant jet. His results showed differences in the predicted drag compared with those of Chou. Kuria [7] attempted to solve the slender body problem in the same way as Chou did, except that he employed a spectral method with modified Chebyshev polynomials. He successfully solved the problem for specific numbers of collocation points.

Nonlinear boundary-element models were developed for cavitating flows about hydrofoils by Uhlman [8,9], and Kinnas and Fine [10,11], among others. They distributed sources and normal dipoles along the body-cavity surface. The unknown values of these sources and dipoles were determined by imposing the dynamic condition on an assumed cavity boundary. The kinematic boundary condition was then used to update the cavity shape.

Beginning in 1994, two numerical hydrodynamics models were developed by the authors for axisymmetric supercavitating high-speed bodies: A slender-body theory model (Varghese et al. [12]) and a boundary-element model (Kirschner et al. [13]; Uhlman et al. [14]). The results of both the slender-body theory model and the boundary-element model have been compared with other numerical and experimental results, with good agreement. Specifically, both models predict the cavity shape and length with good accuracy. The slender-body theory model presented in Varghese et al. [12] is essentially an extension of Chou's method. Viscous drag corrections were incorporated and tested using both the Thwaites and Falkner–Skan approximations along the wet portions of the cavitator, and the effects of subsonic compressible flow were investigated using the compressible Green function. The boundary-element model was employed to examine supercavitating flows past disk-, cone-, and sigma-shaped cavitators. Such predictions are in good agreement with experimental and analytical results, as is summarized, for example, in Savchenko et al. [15].

Several researchers have modeled partially cavitating flows using nonlinear boundary-element techniques (Uhlman [8,9]; Kinnas and Fine [10,11]), but most of this work has addressed only hydrofoils. During preparation of this paper, the authors became aware of boundary-element modeling of axisymmetric flows recently performed in the Former Soviet Union by Krasnov [16]. The formulation of a partial cavitation model for high-speed bodies follows the same methodology used in the supercavitation boundary-element model, wherein sources and normal dipoles are distributed along the body-cavity surface. The unknown values of the source and dipole strengths are then obtained using the mixed Fredholm integral equation that results from the application of Green's third identity. The authors' preliminary formulation and early results of an effort to develop such a method were presented in Varghese [17] and in Varghese and Uhlman [18].

Mathematical Formulation

The physical problem of partial cavitation is shown in Fig. 1. The cavitator shown in this figure is a disk, but the model is capable of handling general axisymmetric cavitator and body geometries. The body length is ℓ_b and the cavity length is ℓ_c. For the partially cavitating case, the body extends beyond the cavity closure point. The bodies considered in this article consist of a truncated circular cone frustum followed downstream by a right circular cylinder. The upstream face of the truncated cone frustum abuts the downstream face of the cavitator. The maximum diam-

Contributed by the Fluids Engineering Division for publication on the JOURNAL OF FLUIDS ENGINEERING. Manuscript received by the Fluids Engineering Division November 2, 2002; revised manuscript received November 20, 2003. Review Conducted by: S. Ceccio.

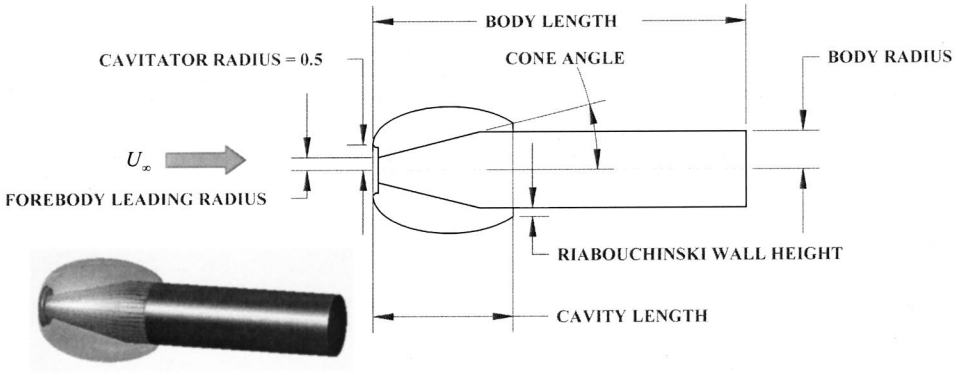

Fig. 1 Partial cavitation problem

eter of the cone frustum is equal to the diameter of the cylinder, which terminates in a flat base. For the bodies discussed herein, the diameter of the upstream face of the truncated cone frustum is equal to the diameter of the cavitator. The edge of the disk cavitator always defines a salient locus of separation. As is discussed below, under certain conditions cavities can originate at points along the body profile other than the cavitator; however, the cavities that have been studied here originate from the edge of the cavitator. The body radius is defined as the radius of the cylindrical portion of the hull. The forebody cone angle is the semiangle of the conical portion of the body and the cone–cylinder intersection is the location where the body changes from a conical to a cylindrical shape.

Much technical literature has been devoted to the conditions at cavity closure, where simultaneous satisfaction of the dynamic and kinematic boundary conditions requires special treatment. (See, for example, Tulin [19].) For the current investigation, the cavity is closed with a modified Riabouchinski cavity termination wall. (Application of this termination model for the axisymmetric boundary-element method is discussed in detail in Kirschner et al. [13]. An improved re-entrant jet closure model is presented in Uhlman et al. [14].)

All quantities in the following formulation have been made dimensionless with respect to fluid density, cavitator diameter, and free-stream velocity. The flow field is governed by Laplace's equation

$$\nabla^2\Phi = 0$$

The total potential, Φ, is the sum of free-stream potential and the disturbance potential, ϕ

$$\Phi = x + \phi$$

The disturbance potential also obeys Laplace's equation.

The disturbance potential satisfies Green's third identity. Thus, with the normal directed out of the fluid, the disturbance potential at any point on the body-cavity surface can be computed from

$$2\pi\phi(\mathbf{x}) = -\iint_S \left[\phi(\mathbf{x}')\frac{\partial}{\partial n}G(\mathbf{x},\mathbf{x}') - G(\mathbf{x},\mathbf{x}')\frac{\partial}{\partial n}\phi(\mathbf{x}')\right] dS(\mathbf{x}') \quad (1)$$

where the Green's function, G, is

$$G(\mathbf{x},\mathbf{x}') = \frac{1}{|\mathbf{x}-\mathbf{x}'|}$$

The dynamic condition on the cavity boundary is derived from Bernoulli's equation, which can be used to derive the following expression for the total velocity along the cavity surface, U_s:

$$U_s = \sqrt{1+\sigma} \quad (2)$$

where σ is the cavitation number. A dynamic condition for the potential on the cavity boundary results by integrating Eq. (2) downstream along the cavity boundary from the cavity detachment point. The kinematic boundary condition specifies that no flow cross the body-cavity boundary

$$\frac{\partial\phi}{\partial n} = -n_x \quad (3)$$

The no net flux condition

$$\iint_S \frac{\partial\phi(x)}{\partial n} dS = 0 \quad (4)$$

is also required to make the problem determinate.

The solution is determined iteratively starting with an initial approximation for the cavity shape, which can be as simple as a straight line from the edge of the cavitator to the outboard end of a small (but otherwise arbitrary) Riabouchinski wall. The panels are distributed along the cavitator, the cavity, the Riabouchinski wall, and the vehicle body aft of the cavity. By imposing the dynamic condition over the cavity boundary [specified as the integration of Eq. (2) downstream along the cavity boundary from the cavity detachment point], applying Green's third identity [Eq. (1)] at all panels along the body-cavity surface, and imposing the no-net-flux condition [Eq. (4)] on all wet surfaces, a system of equations is obtained. This system is solved for the disturbance potential along the wet portions of the boundary and on the Riabouchinski wall, the normal derivative of the disturbance potential along the cavity boundary, and the quantity $\sqrt{1+\sigma}$. Whereas in physical experiments the cavity length is a result of the cavitation number associated with the operating conditions, in the current method it is convenient to specify the cavity length and compute the cavitation number as part of the solution. The cavity length can then be predicted for a specified cavitation number via iteration, if desired. Once the solution is obtained, the cavity shape is updated to satisfy the kinematic condition, Eq. (3), and the Riabouchinski wall height is adjusted accordingly to form a closed profile. The iterations continue until the cavity shape has converged. A flow chart of this computational procedure is presented in Uhlman et al. [14]. Nonuniform panel spacing is used in many locations, in order to reduce the number of panels without reducing the accuracy of the solution. The number of panels along the Riabouchinski wall is allowed to vary as the wall height changes with iteration on cavity geometry. To ensure good accuracy of the results, the distribution of panels along the wet afterbody is modified as well, such that the ratio of neighboring panel lengths is constrained to values between 0.5 and 2.0.

From the converged disturbance potential along the body-cavity surface, the disturbance velocity components are calculated as

$$u_x = \frac{\partial \phi}{\partial x} \quad \text{and} \quad u_r = \frac{\partial \phi}{\partial r}.$$

The total drag coefficient of a partially cavitating body is computed as the sum of the pressure drag and the viscous drag. For the configurations of interest in this article, the pressure drag can be additionally subdivided into two components: (1) A component due to the pressure acting over the cavitator and the body forward of the base; and, (2) the drag due to the pressure acting on the base of the cylinder. With this breakdown, the pressure force is computed by integrating the product of the pressure and the axial component of the local unit normal vector over the cavitator and the body forward of the cylinder–base intersection. For short cavities, the forward part of the body is subject to cavity pressure, and a variable pressure acts downstream of the cavity closure point. For longer cavities, more of the body is subject to cavity pressure. At low enough values of the cavitation number, the cavity is large enough to envelope the entire forebody, so that the forebody is subject to the constant value of cavity pressure over its entire length. Note that, under certain conditions, a second cavity could form at the cone-cylinder intersection. However, for the relatively gentle cone angles considered herein, it is assumed that the flow in this region is more likely to separate than to cavitate, justifying the assumption of a single cavity originating at the cavitator.

The pressure acting at the base of the cylindrical portion of the body depends on the conditions of the flow and the operation of the model under consideration. For an unventilated system, the base flow can cavitate or not, depending on the cavitation number. For example, at high cavitation numbers, the flow will separate at the cylinder–base intersection, allowing the velocity to remain finite in this region without formation of a cavity. In this condition, the time-averaged pressure acting over the base is greater than vapor pressure and relatively constant. The base drag may be approximated from semiempirical formulas available in the technical literature for base-separated flows. (See, for example, Hoerner [20].) To complicate the analysis, cavities can be ventilated; moreover, in the partially cavitating case, the ventilation conditions at the base need not be identical to those at the cavitator. Finally, at very low values of the cavitation number, a supercavity will form that envelopes the entire body, and the pressure acting on the base is simply cavity pressure. Thus, the general flow case requires consideration of a large number of combinations of conditions, an undertaking that was beyond the scope of the current investigation. However, for the important case of nonventilated base flow, for which the base pressure cannot fall below vapor pressure, the base drag is bounded above by its value in the base-cavitating flow condition. Conversely, since pressure recovery over the base is limited by separation, the base drag is bounded below by its value in the base-separated flow condition. For the vaporous base cavitation, as the cavitation number decreases, a ring cavity will form over the outboard region of the base, so there exists a range of the cavitation number over which the base drag will take some intermediate value between the lower bound represented by the value for base-separated flow and the upper bound represented by the value for base-cavitating flow. As the cavitation number continues to decrease, eventually the base cavity will grow to cover the entire base, and the value of the base drag coefficient can be computed by integrating the base cavity pressure over the base. This effect will be discussed in more detail below, in the context of some specific results.

The pressure can be computed from Bernoulli's equation

$$C_p = 1 - q^2$$

where q is the magnitude of the dimensionless local fluid velocity vector. The pressure contribution to the drag coefficient (exclusive of base drag) may then be computed as

$$C_{D\mathrm{p}} = \frac{4}{\pi} \oint_S C_p n_x dS$$

The viscous contribution to the drag coefficient along the wet portions of the conical and cylindrical body areas is calculated using the ITTC equation (see, for example, Newman [21]) for the friction coefficient, c_f. The viscous drag is

$$C_{Dv} = \frac{4}{\pi} \oint_{S_{\mathrm{wetted}}} c_f s_x dS$$

For base-separated flows, the base drag coefficient may be estimated using an empirical formula found in Hoerner [20]

$$C_{Db} = \frac{0.029(2b_{\mathrm{base}})^3}{\sqrt{C_{Dv}}} \tag{5}$$

where b_{base} is the dimensionless body radius at the base. For base-cavitating flows, the base drag coefficient is simply the integral over the base area of the cavity pressure, $p_{c\ \mathrm{base}}$ (which may, in general, be different than the cavity pressure at the cavitator, p_c). This integral can be expressed as

$$C_{Db} = \frac{8 b_{\mathrm{base}}^2 \sigma_{\mathrm{base}}}{\rho U_\infty^2}. \tag{6}$$

With either of these formulas, the total drag coefficient is given by

$$C_D = C_{D\mathrm{p}} + C_{D\mathrm{v}} + C_{D\mathrm{b}}.$$

Results

The model described above was exercised to investigate various effects associated with the body geometry. Selected results are discussed, and (where possible) compared with experimental data found in the technical literature.

Cavity Closure on the Cylindrical Portion of the Body. To isolate the basic effect of body length and radius, a profile was selected with a very short conical forebody, such that the cavity always closed on the cylinder (but not so blunt as to intersect the cavity boundary). These results were compared with the baseline case of supercavitation.

Figure 2 shows cavity shapes for a dimensionless body radius of 0.9 for different values of the cavity length. The dimensionless body length in each of these cases was 40. The cavity length for these cases is plotted against cavitation number in Fig. 3, along with two formulas commonly used to predict the length of supercavities. The first of these formulas is Garabedian's well-known result, derived from first principles, which captures the functional dependence of the cavity length on the cavitation number and on the square root of the drag coefficient (Garabedian [22]):

$$\frac{\ell_{\mathrm{c}}}{d_{\mathrm{c}}} = \frac{1}{\sigma} \sqrt{C_{D\mathrm{c}} \ln \frac{1}{\sigma}}$$

where d_{c} is the cavitator diameter. The second formula plotted in Fig. 3 is a semiempirical result found in May (1975), Eqs. (3)–(13):

$$\frac{\ell_{\mathrm{c}}}{d_{\mathrm{c}}} = \sqrt{C_{Dc}} (1.24 \sigma^{-1.123} - 0.60).$$

May's formula also captures the square-root dependence of cavity length on drag, while the dependence on cavitation number is based on a fit of experimental data. For partial cavitation, as in the case of supercavitation, the cavitation number decreases with increasing cavity length. However, it can be seen that, over most of the range, the cavity at a given cavitation number is shorter for the case of partial cavitation than when the flow is not complicated by the presence of the wet afterbody. The difference between the results for partial cavitation and either of the formulas for super-

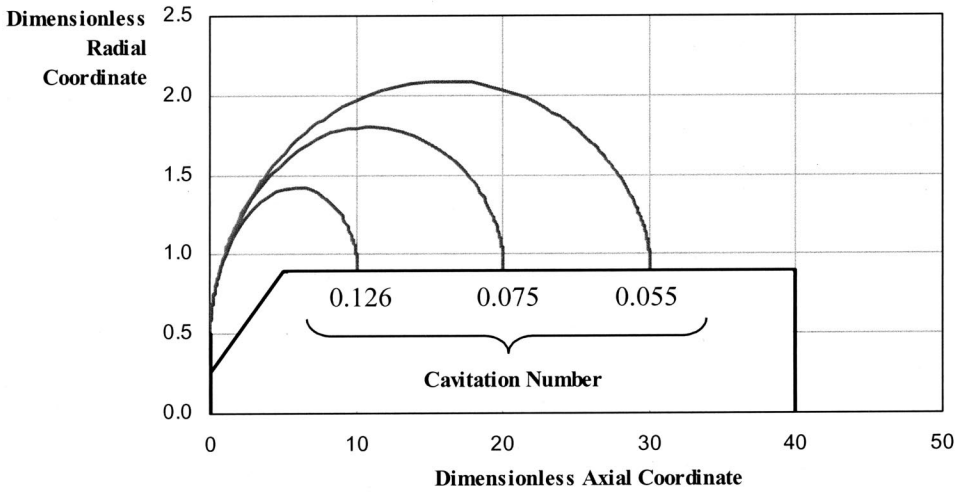

Fig. 2 Cavity shapes for different cavity lengths (dimensionless body radius: 0.9; dimensionless body length: 40)

cavitation is significantly greater than the difference between the two formulas for supercavitation themselves, especially for cavitation numbers greater than $\sigma=0.1$.

An intuitive explanation of the physics underlying this effect is based on the conditions at cavity closure. Although this region is generally unsteady for the axisymmetric flow conditions studied herein, the Riabouchinski wall model approximates the time-averaged cavity behavior by allowing for pressure recovery at the cavity end. In the case of supercavitation, stagnation pressure acts only on the axis of symmetry. For the partially cavitating flow currently considered, however, the locus of stagnation is a circle at the intersection of the Riabouchinski wall and the wet afterbody. Thus, the high-pressure region near cavity closure is more extensive, an effect that leads to shorter cavities.

Further insight concerning these effects can be gleaned from Fig. 4(*a*), which presents surface pressure distributions for a dimensionless body radius of 0.8 for two different values of the partial cavity length and for the case of supercavitation. The plots in Fig. 4(*b*) present the associated body-cavity geometry for the same three flow cases. Figure 4(*a*) also gives an idea of the distribution of panels along the surface. Note the increased panel density where pressure gradients are large. It can be seen that the pressure along the cavitator falls from its value at the stagnation point at the center of the cavitator and is continuous across the edge of the cavitator, at which point the value has dropped to cavity pressure. The pressure rises to its stagnation value at the intersection of the Riabouchinski wall and the body (if the cavity closes on the body) or on the Riabouchinski wall at the axis of symmetry (for a supercavity). For partial cavitation, the pressure coefficient downstream of the cavity closure point gradually approaches zero along the cylindrical body as the flow velocity approaches that of free-stream, then drops rapidly near the base–cylinder intersection. Note that this low-pressure spike should be considered an artifact of the simple model implemented at the base: A more physically realistic approach would properly account for flow separation in that region. The current model is deemed to be acceptable, except when cavity closure occurs very close to the base, at which point the nonphysical localized low pressure at the assumed cylinder-base intersection probably results in cavity lengths that are somewhat overpredicted. Also note that a low-pressure spike is predicted at the cone–cylinder intersection if the cavity closes upstream of this point. In a real flow, viscous effects would lead to a separation bubble at this point, which would tend to mitigate this spike. Alternatively, low pressure in this region

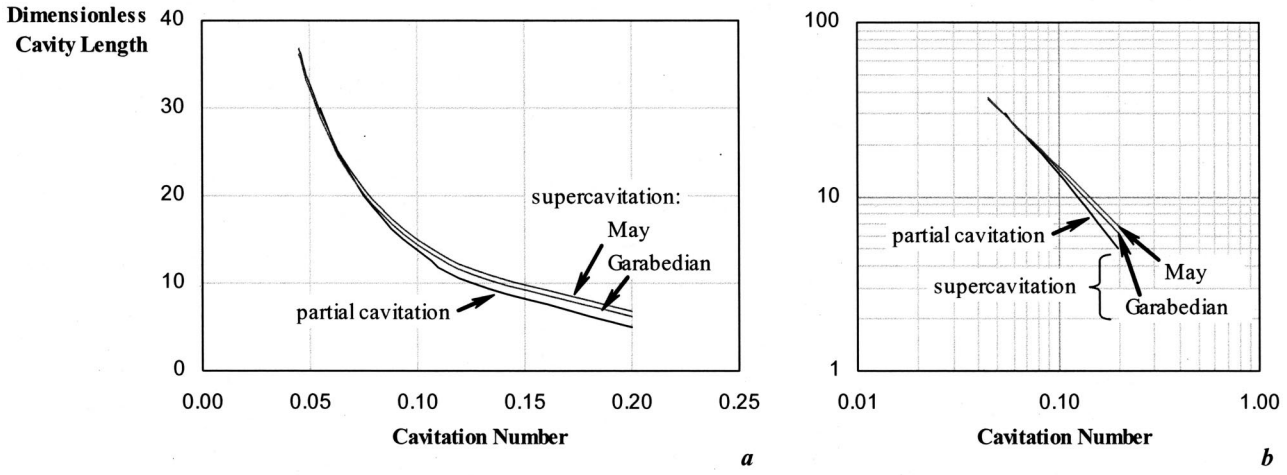

Fig. 3 Cavity length versus cavitation number on (*a*) linear and (*b*) logarithmic scales (dimensionless body radius: 0.9; dimensionless body length: 40)

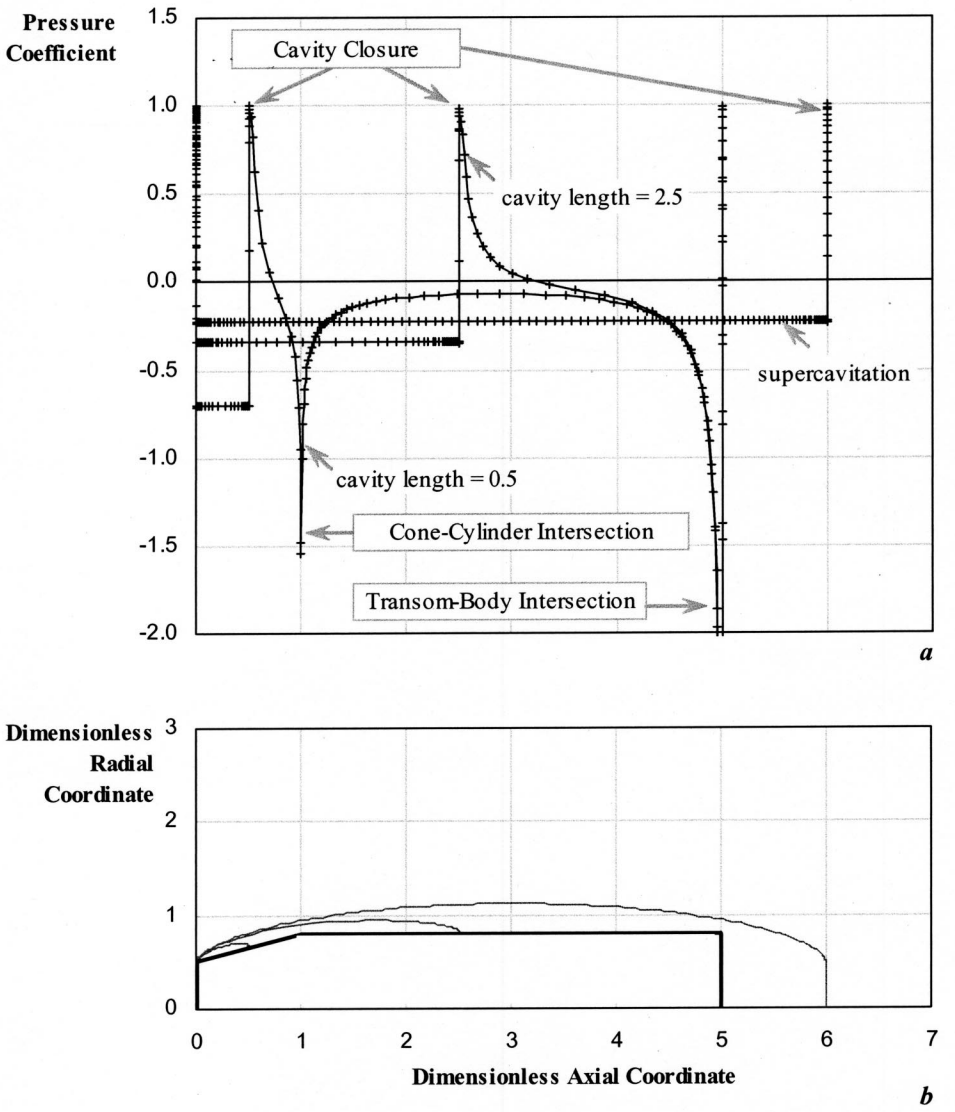

Fig. 4 (*a*) Surface pressure distribution and (*b*) cavity shape for different cavity lengths (dimensionless body length: 5; dimensionless body radius: 0.8); see text for discussion of pressure spikes

could be associated with a second cavity. Neither effect has been addressed with the current model, so it is expected that the cavity length is slightly over-predicted for cases in which closure occurs just upstream of the cone–cylinder intersection.

Figure 5 presents cavity shapes at a constant cavity length for the body radii ranging from 0.5 to 1.3. Here the cavity length is 30 and the body length is 40. Changes in the cavity shape are much more apparent downstream of the point of maximum cavity radius, although significant differences can also be observed somewhat forward of this point.

Figures 6(*a*) and 6(*b*) present the Riabouchinski wall height as a function of the body radius and cavity length, respectively. In Fig. 6(*a*), the Riabouchinski wall height is plotted against the body radius for values of the cavity length of 10, 20, and 30. It can be seen that, for all cavity lengths, the Riabouchinski wall height decreases with increasing body radius. The curves are somewhat jagged, especially for a body radii greater than 1 cavitator diameter. This may be due to discretization error. Figure 6(*b*) shows the variation of Riabouchinski wall height with cavity length for two values of the body radius. The wall height is seen to decrease with increasing cavity length.

The decrease in the Riabouchinski wall height with increasing body radius provides information concerning the maximum body that can be accommodated by a partial cavity for a given cavitation number. With further increase in the body radius, negative values of the Riabouchinski wall height were obtained, so that the converged cavity shape actually intersected the body, suggesting that such a cavity is not physically realizable. Over most of the parameter space studied, this occurred when the body radius was greater than approximately 1.3 times the cavitator diameter (to within the resolution tested; that is, for increments of a dimensionless body radius of 0.1), as is depicted in Fig. 7. When the cavity closure location was very close to the aft end of the body, negative Riabouchinski wall heights occurred at lower values of the body radius; for longer bodies, this effect occurred at lower ratios of the cavity length to the body length. (Note, however, that the results for very long partial cavities—approaching the body length—are not entirely accurate, because cavitation or separation at the base of the cylinder has not been properly modeled. The effects of this deficiency are considered negligible for lower values of the ratio of cavity to body length.)

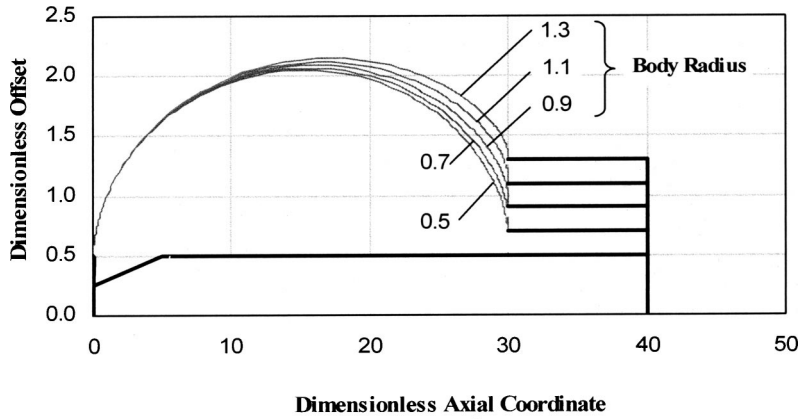

Fig. 5 Cavity shapes for various body radii (dimensionless body length: 40; dimensionless cavity length: 30)

At least from a numerical perspective, limitations also apply to the minimum cavity length for a given body radius. Figure 8 shows the minimum cavity length for which convergence was achieved as a function of the body radius. When the current analysis was applied to flow cases with shorter cavities than this minimum value, nonphysical cavity shapes resulted, characterized by nonconvex profiles. It can be seen that this minimum cavity length increases with increasing body radius.

Figure 9(*a*) presents the cavitation number versus the cavity length for different body radii. The dimensionless body length is again 40. Except for the case of supercavitation (a body radius of zero), the cavity closes on the cylindrical portion of the body. The cavitation number decreases with increasing body radius. As the cavity length increases, each curve asymptotically approaches the supercavitation result, which agrees well with the low-cavitation-number limits of two formulas presented in May [23]. One of these is May's own semiempirical formula, and the other is Garabedian's theoretical formula [22]. A dimensionless body radius of 0.5 is the case where the cavitator and cylinder diameters are the same, the so-called ''zero-caliber ogive'' for which partial cavitation experiments were performed by Billet and Weir [24]. Figure 9(*b*) presents the cavity length versus cavitation number for this case for the current method (labeled ''0.5''), for the curve fit recommended in [24] for their experimental results:

$$\frac{\ell_c}{d_c} = \left(\frac{0.751}{\sigma}\right)^{1/0.75}$$

and for the semiempirical formula for supercavitation recommended in May [23]. It can be seen that, although the current

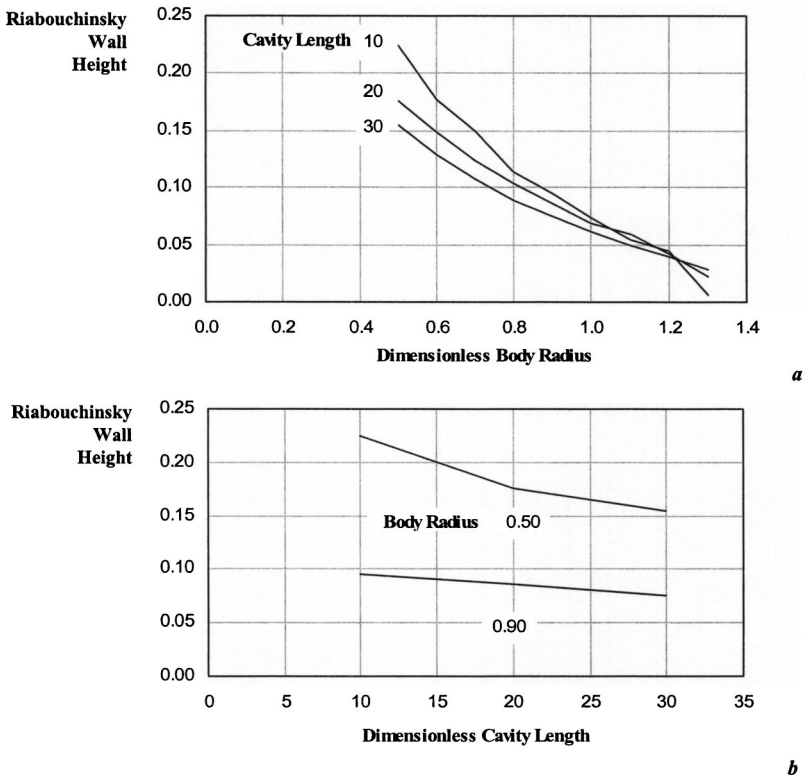

Fig. 6 Riabouchinski wall height versus (*a*) body radius and (*b*) cavity length (dimensionless body length: 40)

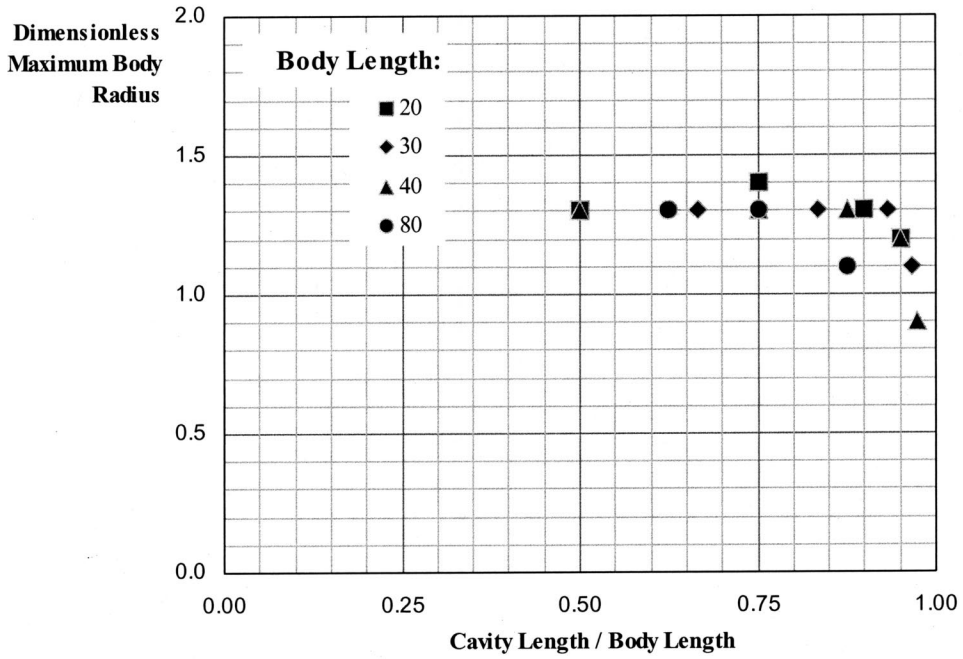

Fig. 7 Maximum body radius (resolved in increments of 0.1) for nonnegative Riabouchinski wall height as a function of cavity length

results fall between the two sets of experimental data, the trend is somewhat closer to the partially cavitating case, suggesting that part of the difference between the data sets presented in [23] and in [24] can be explained by the presence of the body in the latter case. Other differences may be attributable to any difference in body length between the flow case associated with Fig. 9(*b*) and the actual model length of Billet and Weir (1975), which is not stated in their publication. Also, the physical flow conditions at the model base and the presence of a strut and tunnel walls are not accounted for in the current model. Although the presence of a body will be less important for cylinders of the smaller radii, it is suggested that the current method could be used to correct experimental supercavitation data for the presence of a downstream sting.

It is often useful to have available a simple approximate formula relating cavity length to cavitation number. For the case of supercavitation, many such formulas are available, notably Garabedian's theoretical formula [22] and May's semiempirical formula [23] shown in Figs. 3 and 9. Such a formula is proposed in the Appendix for the case of a partial cavity terminating on the cylindrical portion of the body.

Cavity Closure on the Conical Forebody. The pressure distribution for closure on the conical forebody of a selected configuration was discussed above in connection with Fig. 4. Figure 10 presents the effect of the body radius if the cavity closes on the conical portion of the body. It can be seen that a much longer cavity is generated for supercavitation than for the partially cavi-

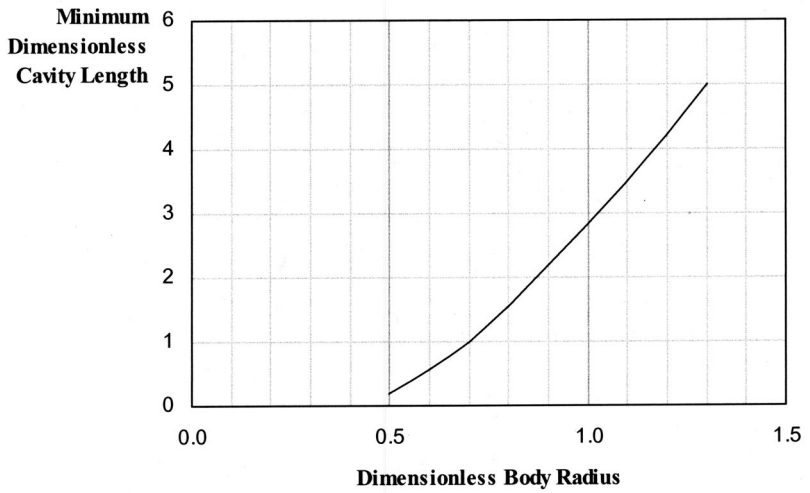

Fig. 8 Minimum cavity length for which convergence was achieved versus body radius (dimensionless body length: 40)

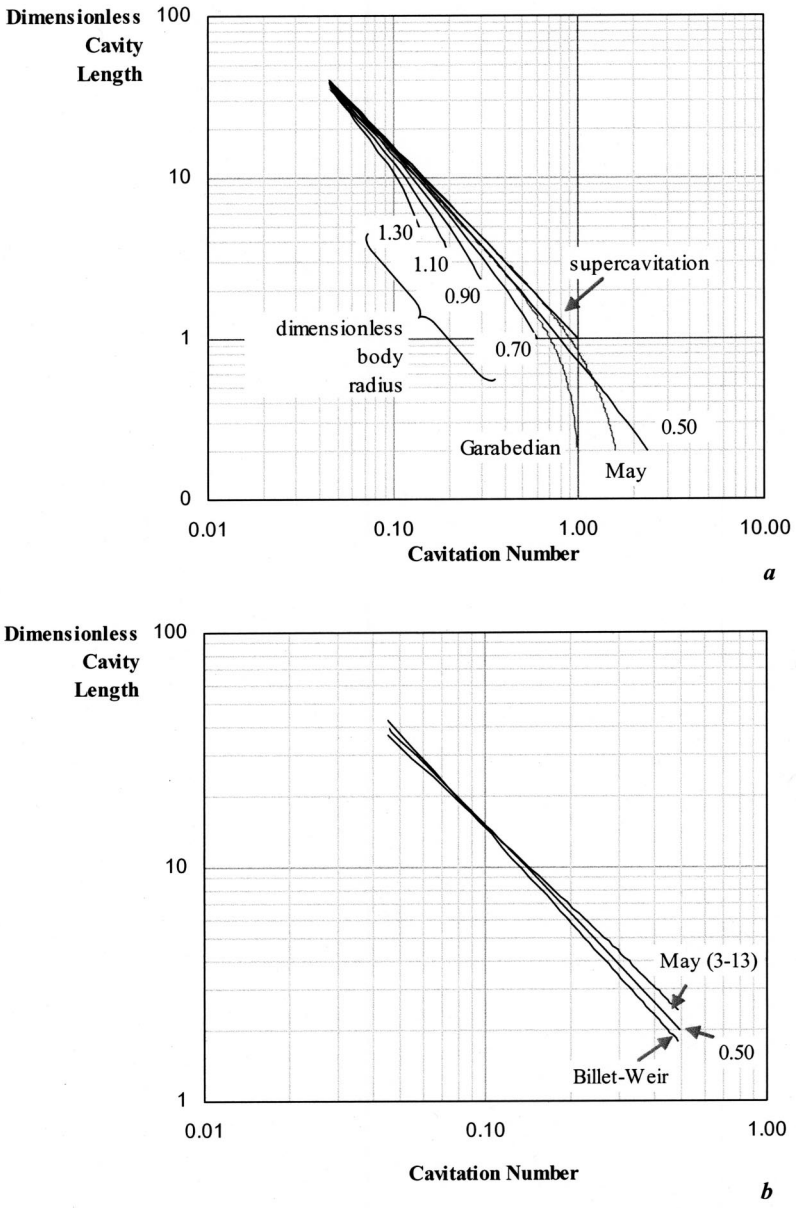

Fig. 9 Cavity length versus cavitation number (*a*) for bodies of different radii (dimensionless body length: 40); (*b*) comparison with the zero-caliber ogive experiments of Billet and Weir (1975)

tating case at the same cavitation number. For a constant cavitation number, the cavity length decreases slightly with increasing body radius, especially at lower cavitation numbers. The semi-empirical results from May [23] are also presented in the figure for purposes of comparison with the case of supercavitation.

In Fig. 11(*a*), the cavitation number versus the cavity length is plotted for three different cone angles: 4.77 deg, 9.55 deg, and 15.92 deg. The dimensionless axial coordinates of the cone–cylinder intersection for each of these bodies are 8.38, 4.16, and 2.46, respectively. The body length is 80 and the cavity closes on either the conical or the cylindrical portion of the body. For cone angles of 4.77 deg and 9.55 deg, a continuous curve is obtained. But for 15.92 deg, the curve is discontinuous for values of the cavity length between approximately 2 and 6.

This can be explained by referring to Fig. 12, where the cavity shapes for different cavitation numbers are shown for this cone angle. The cavity shapes for cavity lengths 4 and 5, even though they are shown in the figure, intersect the body and so are not physically realizable. Hence a jump in the cavity length is required at this point. For the other two cone angles shown in Fig. 11, the cone–cylinder intersection is further downstream, so the cavity is large enough to envelope that point as the cavity length increases continuously with a decrease in the cavitation number; thus continuous curves result. Note, however, the very apparent change in the slopes of the curves, even for the 9.55 deg cone angle, as the cavity closure point moves from the cone to the cylinder in each case. This effect is emphasized in Fig. 11(*b*), where the reciprocal of the cavitation number is plotted versus cavity length for each of the body profiles. This figure clearly shows either discontinuous or slope-discontinuous behavior when the cavity closes at the cone–cylinder intersection, depending on the cone angle.

Although the current analysis does not address ventilation effects, such behavior may be related to the hysteresis effect discussed in Semenenko [25]. This effect, which was discovered and investigated experimentally, involves the behavior of nominally

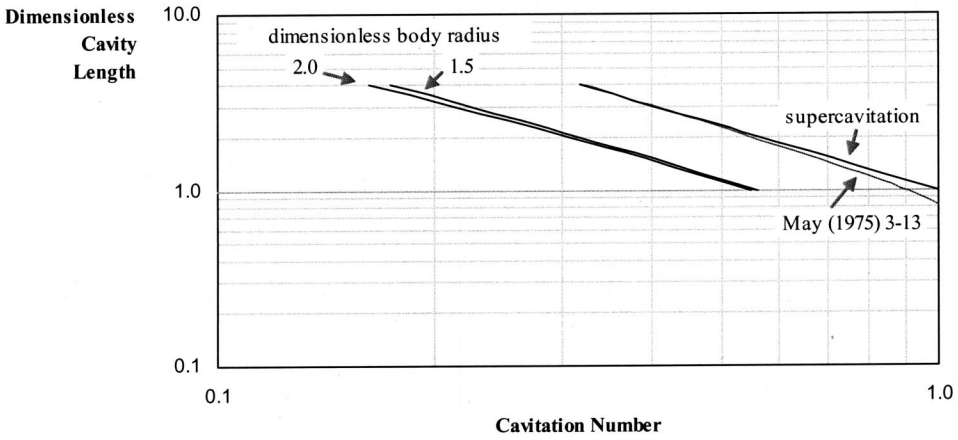

Fig. 10 Cavity length versus cavitation number for cavity termination on the conical forebody, comparing partial cavitation with supercavitation (dimensionless body length: 80; cone angle: 6.96 deg)

axisymmetric ventilated cavities that close on an axisymmetric body profile with slope discontinuities. Specifically, Semenenko claims that the ventilation rate required to maintain a cavity of a given length depends on the angle that the cavity boundary makes with the body profile near closure. Since this quantity depends, in turn, on the slope of the profile and the cavity length, a slope-discontinuous profile is associated with discontinuities in the relationship between the required ventilation rate and the cavity length. Figures 11 and 12 herein provide qualitative evidence of a similar dependence on the angle that the cavity boundary makes with the body profile near closure. This result suggests that the effect discussed in [25] involves the relationship between the cavi-

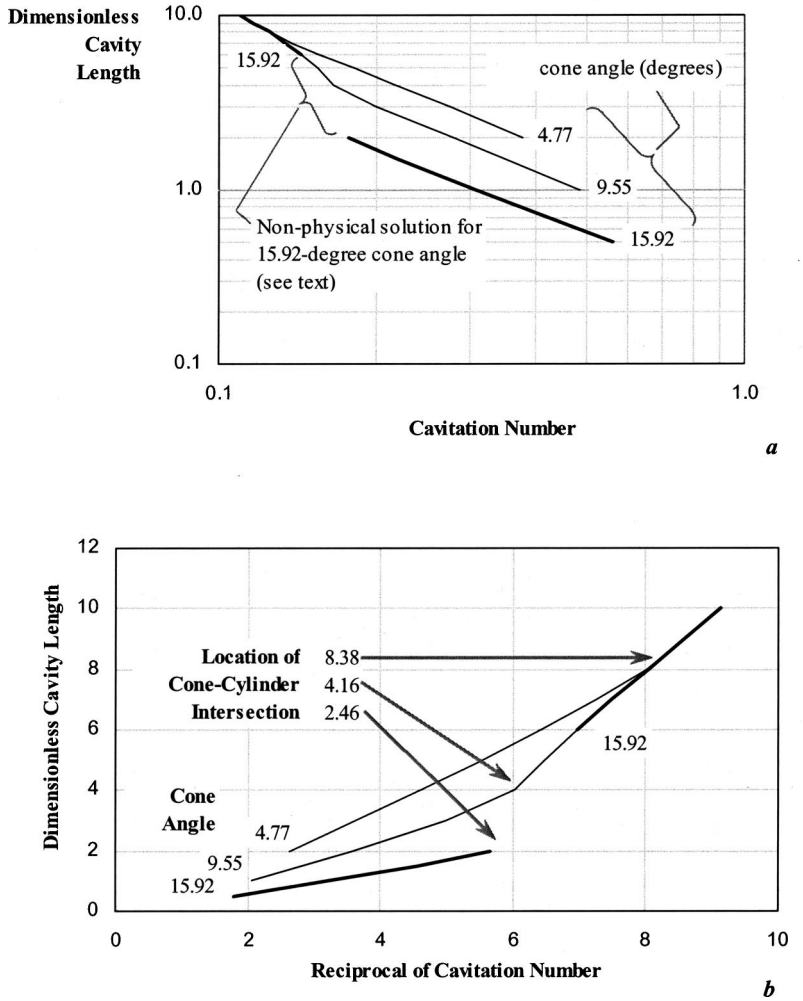

Fig. 11 Cavity length versus (*a*) cavitation number and (*b*) reciprocal of cavitation number for three different cone angles (dimensionless body length: 80; dimensionless body radius: 1.2)

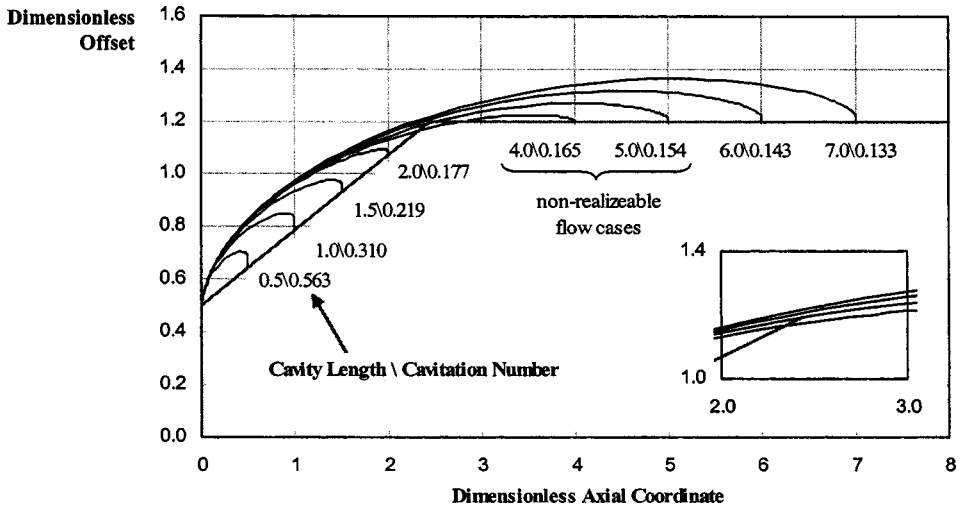

Fig. 12 Numerical analysis of high-speed bodies in partially cavitating flow

tation number and the cavity length directly, although it is clear that the required ventilation rate must also be affected. Application of the current model to the body profiles discussed by Semenenko for purposes of a more direct comparison was beyond the scope of this effort.

Drag coefficients for bodies with cone angles of 9.55 deg and 15.92 deg are plotted in Figs. 13 and 14, respectively, broken down into the components described above. For these examples, it was assumed that the flow at the cylinder base was separated, rather than cavitating, and the base drag component was computed using Eq. (5). The pressure drag in Fig. 13 decreases as the cavity closure point approaches the cone–cylinder intersection and then increases slowly as the cavity length increases. This behavior is reflected in the total drag, since the pressure drag is a significant component, and the other components change only slowly with changes in the cavity length. As is to be expected, the viscous drag decreases with increasing cavity length while the base drag increases. Note that all these computations were performed for a single, arbitrarily selected value of the Reynolds number.

In Fig. 14, the drag associated with the nonphysical solutions for values of the cavity length between 2 and 6 is not shown, although the pressure and total drag coefficients show a tendency toward reduced values just outside this range, so that the qualitative behavior is similar to that described in Fig. 13.

The local minimum in the forebody pressure drag coefficient as the cavity closure point approaches the cone–cylinder intersection represents two primary competing effects: (1) A decrease in the length of the conical forebody that is exposed to elevated pressures downstream of the cavity closure point; and, (2) the increase in cavity pressure relative to ambient as the cavitation number increases, which results in increased drag on the forebody. It can be seen from Fig. 4 that the fraction of the forebody length that is exposed to pressures higher than static pressure is reduced as more of the cone is enveloped by the cavity. Once the cavity

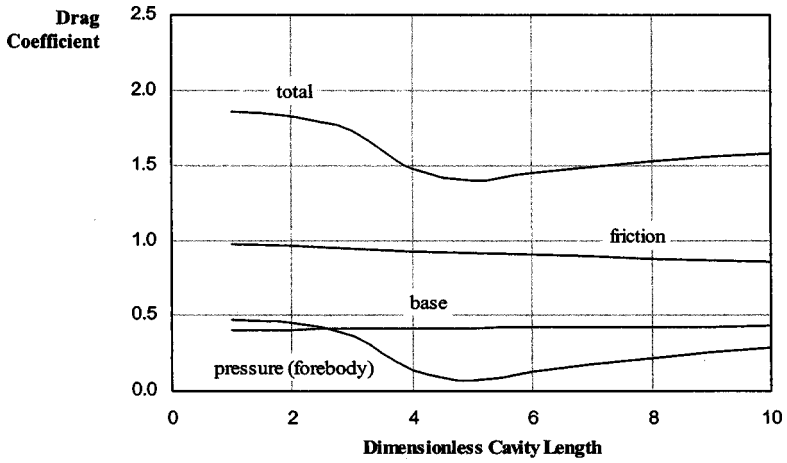

Fig. 13 Drag coefficient versus cavity length (dimensionless body length: 80; dimensionless body radius: 1.2; cone angle: 9.55 deg; Reynolds number: 3.0e7)

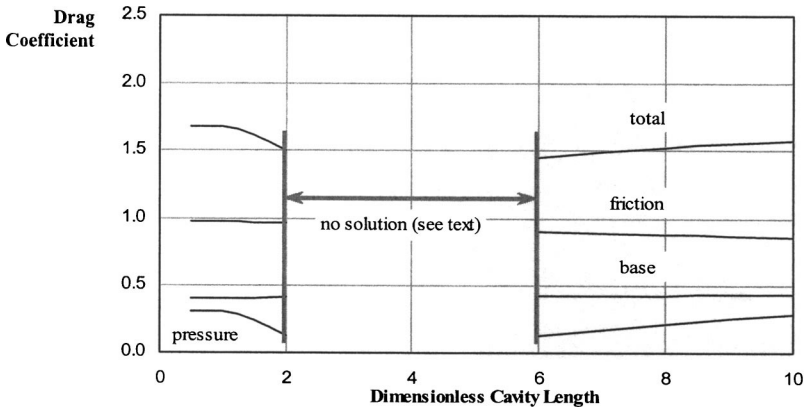

Fig. 14 Drag coefficient versus cavity length (dimensionless body length: 80; dimensionless body radius: 1.2; cone angle: 15.92 deg; Reynolds number: 3.0e7)

closure point reaches the cone–cylinder intersection, no further decrease can occur, since the cone is completely enveloped. The minimum pressure drag should, therefore, be observed when the cavity and cone lengths are equal; the cavity increments used to produce the curves in Fig. 13 were not quite sufficient to resolve the pressure minimum exactly, although the basic behavior is captured. The dip in the total drag coefficient as the cavity closure point approaches the cone–cylinder intersection does not reduce the drag to values associated with supercavitation. In that case, there is no base drag as currently defined, friction drag is negligible, and the total drag is simply the cavitator drag for a disk, so that the total drag coefficient based on cavitator projected area takes a value approaching 0.82–0.84 (see, for example, May [23], Kirschner et al. [13], Uhlman et al. [14], and many others).

Figures 15 and 16 show the effects of body radius when the cavity closes on the conical portion of the body at constant values of the cavitation number. Once again, the base drag was computed using Eq. (5), assuming that the flow is base-separated, rather than base-cavitating. For this example, the cavitation number was fixed at 0.15, the dimensionless body length was 80, and the cone angle was 15.92 deg. As for the case of cavity closure on the cylinder, it can be seen in Fig. 15 that the cavity length decreases with increasing body radius. Figure 16 shows that all the drag components except the pressure drag increase with increasing body radius over the range considered. The increase in friction drag is due to the increase in the ratio of wet area to cavitator area. Similarly, the increase in base drag is associated with the increase in the ratio of base area to cavitator area. The forebody pressure drag varies under the influence of two primary competing effects: (1) The increase in the wet area of the conical forebody that is exposed to elevated pressures downstream of the cavity closure point; and, (2) the increase in the wet area of the conical forebody exposed to the low-pressure spike near the cone–cylinder intersection. At this cavitation number, with the cavity enveloping a fraction of the cone, the first effect leads to a slight increase in the pressure drag coefficient until a dimensionless body radius of approximately 1.8, at which point the effect of the low-pressure spike begins to dominate and the pressure decreases.

The Effect on Drag of Flow Conditions at the Cylinder Base

As discussed above, the base and total drag coefficients depend on the type of flow occurring at the base of the cylinder: Base-separated flow, in which case the base drag is computed using Eq. (5), or the base-cavitating flow, for which Eq. (6) applies. In reality, the base drag coefficient can fall somewhere between these two values, depending on the extent of cavitation over the cylinder base. Thus, the base-separated and base-cavitating flow cases represent limiting values that are useful for the purposes of estimating the total drag on a partially cavitating body.

As an illustration of this behavior, the base and total drag coefficients were predicted for a partially cavitating body with a dimensionless length of 40 and a dimensionless cylinder radius of

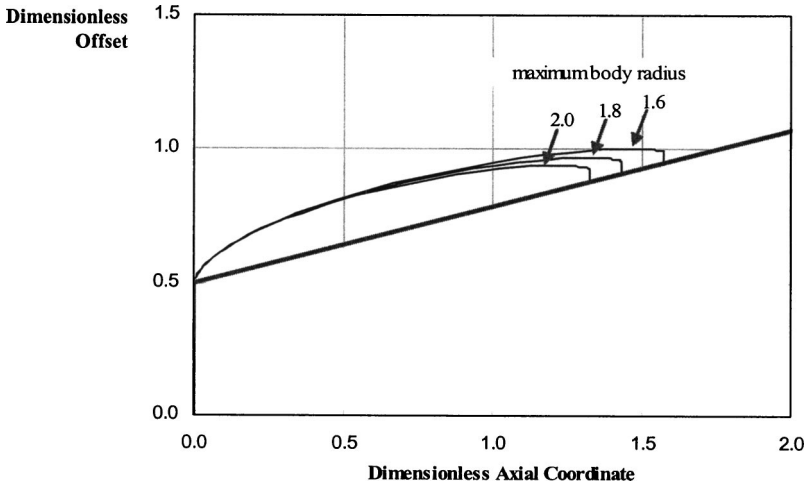

Fig. 15 Cavity shapes for different maximum dimensionless body radii (dimensionless body length: 80; cavitation number: 0.15; cone angle: 15.92 deg)

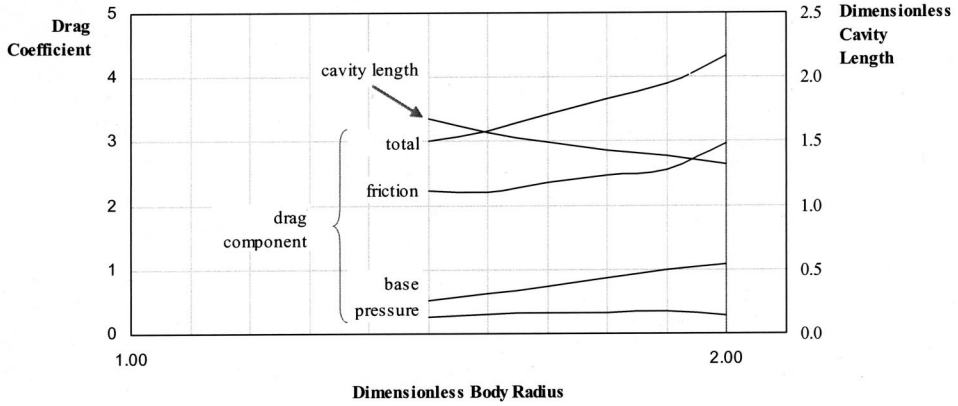

Fig. 16 Dimensionless cavity length and drag components versus dimensionless body radius (dimensionless body length: 80; cavitation number: 0.1; cone angle: 15.92 deg)

0.9, subject to base-separated and base-cavitating flow. For each of these two cases, it was assumed that the forward cavity closed on the cylindrical portion of the body. For the case of the base-cavitating flow, it was assumed that cavity pressure at the base and at the cavitator were equal. The results are presented in Fig. 17.

It can be seen that as the cavitation number decreases with increasing cavity length, the base drag coefficient for the base-cavitating flow case also decreases in accordance with Eq. (6). Assuming that the semiempirical formula, Eq. (5), is applicable, a generally opposite trend applies to the base-separated flow case. These trends are reflected in the total drag coefficients. It is thus apparent from Fig. 17 that the total drag coefficient is very dependent on the base flow conditions. Therefore, in applying these results, several cautions must be noted, as follows:

As discussed above, the pressure in the fluid cannot fall below vapor pressure. Thus, the base drag coefficient cannot achieve a value higher than the value computed for the case of the base-cavitating flow with the cavity pressure equal to vapor pressure. Thus for the example results presented in Fig. 17, the base drag coefficient for the base-separated flow case is nonphysical for dimensionless cavity lengths greater than approximately 13.6. For longer cavities, cavitation would begin to occur over the base, and the base drag coefficient would begin to depart from the curve for base separation shown in Fig. 17, and eventually follow the curve for base cavitation as the base flow became fully cavitated. The total drag coefficient is similarly limited.

If the cavities at the cavitator and at the base are subject to unequal values of cavity pressure, as can occur for a ventilated system, results such as those presented in Fig. 17 must be modified.

The results for the base-separated flow case are presented as an engineering approximation based on a semiempirical formula for the drag coefficient. This formula is a rather simplified expression that does not involve body length as a parameter, nor does it account for the occurrence of cavitation. Such complications warrant additional modeling and experimental validation to improve predictions such as those presented in Fig. 17.

Conclusions

A physics-based model of partial cavitation has been developed for axisymmetric flows. The model has been applied to a disk cavitator with a simple body profile consisting of a conical forebody abutting a cylinder. The effects of the body radius and forebody cone angle on the cavity shape and length, the cavitation number, and the body drag were studied. The model predicts that,

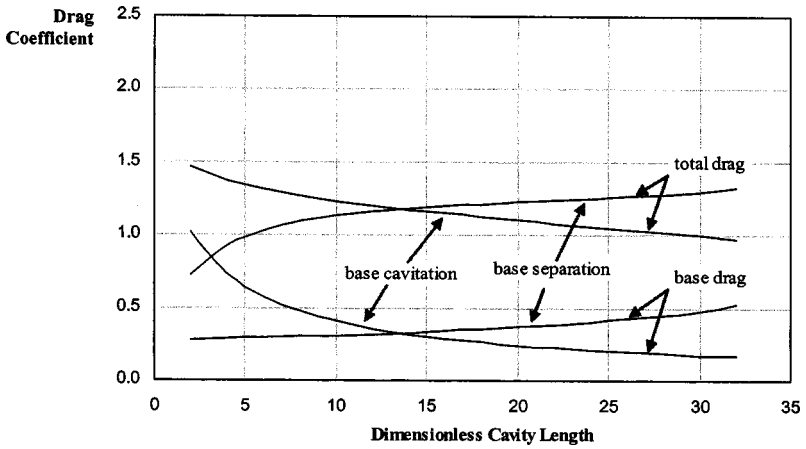

Fig. 17 Base and total drag coefficients versus cavity length (dimensionless body length: 40; dimensionless body radius: 0.9; Reynolds number: 3.0e7) comparing the base-separated and base-cavitating flow cases

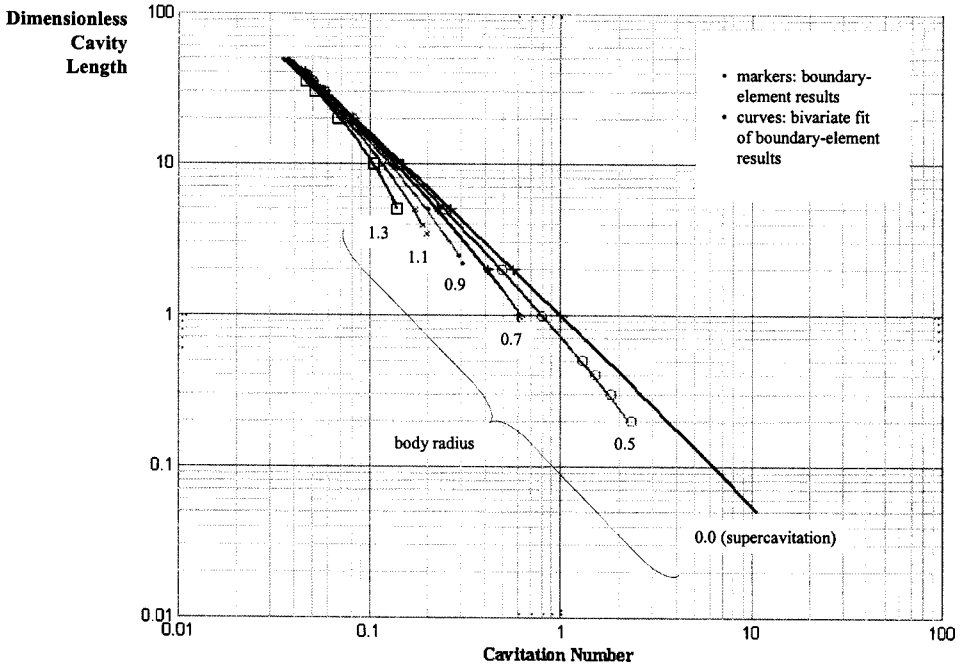

Fig. 18 Bivariate surface fit of cavity length as a function of cavitation number and cylinder radius (results strictly applicable to a dimensionless body length of 40; computed using Eq. (7); original numerical data plotted as markers)

for fixed cavitation number, partial cavities are generally shorter than supercavities for the same cavitation number over the regime investigated. The model also predicts that, for a given cavitation number, cavity length decreases and drag increases with an increase in the body radius over most of the parameter space investigated. A dip in the pressure drag coefficient occurs as the cavitation number decreases and the cavity termination point approaches the cone–cylinder intersection. However, discontinuous cavity behavior can also occur at such an operating point, depending on the forebody cone angle. It is proposed that this effect is related to experimental observations of other researchers involving ventilation hysteresis effects.

Acknowledgments

This work was supported, in part, by the Office of Naval Research (ONR), most recently with the sponsorship of Dr. K. Ng under Program No. 0602747N. Previous support was provided by Mr. J. Fein, then of ONR.

Nomenclature

A_c = cavitator projected area
$b(x)$ = body-cavity radius at axial location x
b_{base} = radius of cylindrical portion of body
b_{ij} = coefficients used in surface fit of computed results
C_D = total drag coefficient, $D/\frac{1}{2}\rho U_\infty^2 A_c$
C_{Db} = base (pressure) drag coefficient, $D_b/\frac{1}{2}\rho U_\infty^2 A_c$
C_{Dc} = cavitator drag coefficient for a supercavity, $D_c/\frac{1}{2}\rho U_\infty^2 A_c$
C_{Dp} = pressure drag coefficient, $D_p/\frac{1}{2}\rho U_\infty^2 A_c$
C_{Dv} = viscous drag coefficient, $D_v/\frac{1}{2}\rho U_\infty^2 A_c$
C_f = friction coefficient, $\tau_w/\frac{1}{2}\rho U_\infty^2$
C_p = pressure coefficient, $(p-p_\infty)/\frac{1}{2}\rho U_\infty^2$
D = total drag on the body
D_b = base drag at the aft end of the body
D_c = cavitator drag for a supercavity
D_p = pressure drag on the body excluding base drag component
D_v = viscous drag on the body
d_c = cavitator diameter
ℓ_b = body length
ℓ_c = cavity length
$\ell_i(b)$ = coefficients used in surface fit of computed results
p_c = cavity pressure at cavitator
$p_{c\ \text{base}}$ = cavity pressure at cylinder base, for base-cavitating flows
p_∞ = free-stream ambient pressure
q = magnitude of local fluid velocity vector
s = arc length coordinate along body-cavity surface
U_∞ = free-stream velocity
x = axial distance
ρ = density of water
σ = cavitation number, $(p_\infty-p_c)/\frac{1}{2}\rho U_\infty^2$, based on cavity pressure at cavitator
σ_{base} = cavitation number, $(p_\infty-p_{c\ \text{base}})/\frac{1}{2}\rho U_\infty^2$, based on cavity pressure at cylinder base
Φ = total potential
ϕ = disturbance potential

Appendix: Parametric Surface Fit of Partial Cavity Characteristics

It is often useful to have available a simple approximate formula relating the cavity length to the cavitation number. For the case of partial cavitation over a cylindrical body of dimensionless length of 40, the following surface is proposed, based on curve fits of the numerical results presented above

$$\ln(\sigma(\ell_c,b)) = \ell_1(b)\ln^2(\ell_c) + \ell_2(b)\ln(\ell_c) + \ell_3(b) \quad (A\text{-}1)$$

where b is the cylinder radius

$$\ell_i(b) = b_{i1}b^2 + b_{i2}b + b_{i3}$$

and

$$b_{ij} = \begin{bmatrix} -0.0648 & 0.5201 & -1.0961 \\ -0.0003 & -0.0210 & 0.0899 \\ -0.0069 & -0.8140 & -0.0031 \end{bmatrix}$$

The minimum cavity length for which the formula is applicable is given as a polynomial regression to the results presented in Fig. 18

$$\ln(\ell_{c\ \min}) = -2.0717\ln^2(b) + 2.4282\ln(b) + 1.0842 \quad (A\text{-}2)$$

The original data computed using the boundary-element method is compared in Fig. 18 with the associated family of curves generated using Eq. (*A*-1). It can be seen that the surface fit is quite satisfactory for values of the cavity length greater than the minimum defined by Eq. (*A*-2).

References

[1] Efros, D. A., 1946, ''Hydrodynamic Theory of Two-Dimensional Flow With Cavitation,'' Dokl. Akad. Nauk SSSR, **51**, pp. 267–270.

[2] Tulin, M. P., 1964, ''Supercavitating Flows—Small Perturbation Theory,'' J. Ship Res., **7**, p. 3.

[3] Cuthbert, J., and Street, R., 1964, ''An Approximate Theory for Supercavitating Flow About Slender Bodies of Revolution,'' LMSC Report, TM81-73/39, Lockheed Missiles and Space Co., Sunnyvale, CA.

[4] Brennan, C., 1969, ''A Numerical Solution of Axisymmetric Cavity Flows,'' J. Fluid Mech., **37**, p. 4.

[5] Chou, Y. S., 1974, ''Axisymmetric Cavity Flows Past Slender Bodies of Revolution,'' J. Hydronautics, **8**, p. 1.

[6] Vorus, W. S., 1991, ''A Theoretical Study of the Use of Supercavitation/Ventilation for Underwater Body Drag Reduction,'' VAI Technical Report, Vorus & Associates, Inc., Gregory, MI.

[7] Kuria, I. M., Kirschner, I. N., Varghese, A. N., and Uhlman, J. S., 1997, ''Compressible Cavity Flows Past Slender Non-Lifting Bodies of Revolution,'' *Proceedings of the ASME & JSME Fluids Engineering Annual Conference & Exhibition, Cavitation and Multiphase Flow Forum*, FEDSM97-3262, Vancouver, BC.

[8] Uhlman, J. S., 1987, ''The Surface Singularity Method Applied to Partially Cavitating Hydrofoils,'' J. Ship Res., **31**, p. 2.

[9] Uhlman, J. S., 1989, ''The Surface Singularity or Boundary Integral Method Applied to Supercavitating Hydrofoils,'' J. Ship Res., **33**, p. 1.

[10] Kinnas, S. A., and Fine, N. E., 1990, ''Nonlinear Analysis of the Flow Around Partially and Super-Cavitating Hydrofoils by a Potential Based Panel Method,'' *Proceedings of the IABEM-90 Symposium*, International Association for Boundary Element Methods, Rome, Italy.

[11] Kinnas, S. A., and Fine, N. E., 1993, ''A Numerical Nonlinear Analysis of the Flow Around Two- and Three-Dimensional Partially Cavitating Hydrofoils,'' J. Fluid Mech., **254**, pp. 151–181.

[12] Varghese, A. N., Uhlman, J. S., and Kirschner, I. N., 1997, ''Axisymmetric Slender-Body Analysis of Supercavitating High-Speed Bodies in Subsonic Flow,'' *Proceedings of the Third International Symposium on Performance Enhancement for Marine Applications*, T. Gieseke, editor, Newport, RI.

[13] Kirschner, I. N., Uhlman, J. S., Varghese, A. N., and Kuria, I. M., 1995, ''Supercavitating Projectiles in Axisymmetric Subsonic Liquid Flows,'' *Proceedings of the ASME & JSME Fluids Engineering Annual Conference & Exhibition, Cavitation and Multiphase Flow Forum*, FED 210, J. Katz and Y. Matsumoto, editors, Hilton Head Island, SC.

[14] Uhlman, J. S., Varghese, A. N., and Kirschner, I. N., 1998, ''Boundary Element Modeling of Axisymmetric Supercavitating Bodies,'' *Proceedings of the 1st Symposium on Marine Applications of Computational Fluid Dynamics, Hydrodynamic/Hydroacoustic Technology Center*, McLean, VA.

[15] Savchenko, Y. N., Semenenko, V. N., Naumova, Y. I., Varghese, A. N., Uhlman, J. S., and Kirschner, I. N., 1997, ''Hydrodynamic Characteristics of Polygonal Contours in Supercavitating Flow,'' *Proceedings of the Third International Symposium on Performance Enhancement for Marine Applications*, T. Gieseke, editor, Newport, RI.

[16] Krasnov, V. K., 2002, ''The Movement of an Axisymmetrical Solid With Formation of a Cavity,'' *Proceedings of the 2002 International Summer Scientific School on High-Speed Hydrodynamics*, Chuvash National Academy of Science and Art, Cheboksary, Russia.

[17] Varghese, A. N., 1999, ''Boundary-Element Modeling of Partial Cavitating and Supercavitating High-Speed Bodies,'' presentation in the *Proceedings of the 1999 ONR Workshop on Supercavitating High-Speed Bodies*, Naval Undersea Warfare Center, Newport, RI.

[18] Varghese, A. N., and Uhlman, J. S., 2000, ''Advanced Physics Modeling of Supercavitating High-Speed Bodies,'' in ''FY99 Annual In-House Laboratory Independent Research Annual Report,'' NUWC-NPT Working Memorandum 8007 dated 17 April, Naval Undersea Warfare Center Division, Newport, RI.

[19] Tulin, M. P., 2001, ''Supercavitation: An Overview,'' *Lecture Notes for the RTO AVT/VKI Special Course on Supercavitating Flows*, von Karman Institute for Fluid Dynamics, Rhode Saint Genèse, Belgium.

[20] Hoerner, S. F., 1965, *Fluid-Dynamic Drag*, Hoerner Fluid Dynamics, Brick Town, NJ.

[21] Newman, J. N., 1980, *Marine Hydrodynamics*, The MIT Press, Cambridge, MA.

[22] Garabedian, P. R., 1956, ''Calculation of Axially Symmetric Cavities and Jets,'' Pac. J. Math., **6**, pp. 611–689.

[23] May, A., 1975, ''Water Entry and the Cavity-Running Behavior of Missiles,'' SEAHAC Technical Report 75-2, Naval Surface Weapons Center, White Oak Laboratory, Silver Spring, MD.

[24] Billet, M. L., and Weir, D. S., 1975, ''The Effect of Gas Diffusion on the Flow Coefficient for a Ventilated Cavity,'' J. Fluids Eng., December issue, American Society of Mechanical Engineers, New York, NY.

[25] Semenenko, V. N., 2001, ''Artificial Supercavitation: Physics and Calculation,'' *Lecture Notes for the RTO AVT/VKI Special Course on Supercavitating Flows*, von Karman Institute for Fluid Dynamics, Rhode Saint Genèse, Belgium.